The Astronomical Journal, 160:37 (12pp), 2020 July https://doi.org/10.3847/1538-3881/ab94c2

Effective Opacity of the Intergalactic Medium from Galaxy Spectra Analysis

Jose S. Monzon[1], J. Xavier Prochaska[1], Khee-Gan Lee[2], and John Chisholm[1,3]

[1] Kavli Institute for the Physics and Mathematics of the Universe (WPI), University of Tokyo, Kashiwa 277-8583, Japan; jsmonzon@ucsc.edu

[2] University of California, Santa Cruz, 1156 High St., Santa Cruz, CA 95064, USA

Received 2019 November 8; revised 2020 May 7; accepted 2020 May 18; published 2020 June 24

Abstract

We measure the effective opacity ($\tau_{\rm eff}$) of the intergalactic medium from the composite spectra of 281 Lyman-break galaxies in the redshift range $2 \lesssim z \lesssim 3$. Our spectra are taken from the COSMOS Lyα Mapping And Tomographic Observations survey derived from the Low Resolution Imaging Spectrometer on the W.M. Keck I telescope. We generate composite spectra in two redshift intervals and fit them with spectral energy distribution (SED) models composed of simple stellar populations. Extrapolating these SED models into the Lyα forest, we measure the effective Lyα opacity ($\tau_{\rm eff}$) in the $2.02 \leqslant z \leqslant 2.44$ range. At $z = 2.22$, we estimate $\tau_{\rm eff} = 0.159 \pm 0.001$ from a power-law fit to the data. These measurements are consistent with estimates from quasar analyses at $z < 2.5$ indicating that the systematic errors associated with normalizing quasar continua are not substantial. We provide a Gaussian processes model of our results and previous $\tau_{\rm eff}$ measurements that describes the steep redshift evolution in $\tau_{\rm eff}$ from $z = 1.5$–4.

Unified Astronomy Thesaurus concepts: Intergalactic medium (813); Intergalactic gas (812); Lyman-break galaxies (979)

1. Introduction

The intergalactic medium (IGM) is a diffuse gas, mainly consisting of ionized hydrogen and helium, that permeates the space between galaxies in the large-scale cosmic web. The gas is highly ionized by the extragalactic ultraviolet background (EUVB) radiation field and takes the form of a diffuse, $T \sim 10^4$ K plasma. The trace fraction of hydrogen gas that remains neutral ($\chi_{\rm H\,I}$) is responsible for attenuating the radiation from the EUVB and producing the Lyα forest (see McQuinn 2016 for a review). Studies on the Lyα forest have meshed well with cosmological theory as it is the IGM, and not the galaxies it surrounds, that governs the large-scale structure of the universe. It is considered one of the most powerful cosmological probes at $z \geqslant 2$ as it holds the majority of baryons at all epochs (e.g., Becker et al. 2007)

Gunn & Peterson (1965) were the first to discern that a universe filled with neutral hydrogen (H I) would be opaque in the far-UV, especially at higher redshifts, where it is densest. Analyzing the spectrum of any distant, rest-frame UV-emitting object directly points to a fluctuating and photoionized gas that at a given redshift varies considerably from sight-line to sight-line (Shapley et al. 2003). A series of studies (e.g., Dall'Aglio et al. 2008; Faucher-Giguere et al. 2008; Becker et al. 2013) has since carried out careful measurements of how H I evolves to place statistical constraints on properties like density, temperature, and composition. A solid understanding of the physical state of the IGM allows for subsequent research investigating the galaxy formation (Hassan et al. 2020), the ionization history (Theuns et al. 2002; Bernardi et al. 2003; Kirkman et al. 2005), and ultimately the constraints on our leading cosmological theories (Rauch 1998; Becker et al. 2007).

Studies of the physical properties of the IGM have primarily come from the analysis of the mean optical depth of H I (τ) observed in the spectra of distant quasi-stellar objects (QSOs; Kirkman et al. 2005; Becker et al. 2007; Faucher-Giguere et al. 2008; Prochaska et al. 2009). QSO's peak in the UV because of their hot accretion disks (active galactic nucleus; Meiksin 2009). As a QSO's radiation traverses the space between galaxies, a series of absorption lines populate the rest-frame spectrum blueward of 1215 Å. Because the IGM is inhomogeneous, photons interact with the intervening gas at different redshifts, causing absorption features across a multitude of wavelengths; the so-called Lyα forest. For sufficiently distant objects ($z > 5$), where the IGM is the densest (McDonald et al. 2006), the absorption lines become so numerous that more than 70% of the flux is absorbed in the Lyα forest (∼1020–1210 Å).

One can directly measure values describing the attenuation from the spectra of distant objects by estimating the underlying continuum, a process that becomes increasingly difficult at higher redshifts (e.g., Kirkman et al. 2005). QSOs are much brighter and therefore easier to observe at higher redshifts, but the Lyα forest can be observed in the spectra of any distant, UV-emitting source. In fact, the $z > 4$ EUVB is thought to be dominated by a population of faint UV-emitting galaxies in addition to bright QSOs at $g \sim 23$ magnitudes (Lee et al. 2014). Their contribution to the EUVB is caused by the young and massive stars they harbor. We set out to measure the effective Lyα opacity of the IGM, $\tau_{\rm eff}$ using the spectra of these Lyman-break galaxies (LBGs) by exploiting their high number density (Lee et al. 2018, hereafter L18).

LBGs are star-forming galaxies whose emission peak in the rest-frame UV and are selected based on their emission blueward of Lyα in a given filter set (Steidel et al. 1996). The original term "LBG" describes star-forming galaxies selected at $z \geqslant 3$ by their IGM absorption, but the COSMOS Lyα Mapping And Tomographic Observations (CLAMATO) team uses the term to cover all $z \geqslant 2$ galaxies with a far-UV continuum. The stacked spectra of LBGs have been used to constrain the dust attenuation curve (Reddy et al. 2016) and investigate spectral features attributable to hot stars, H II regions and outflowing gas (Shapley et al. 2003). Thomas et al. (2017) analyzed galaxy spectra to estimate $\tau_{\rm eff}$ at

[3] Hubble Fellow.

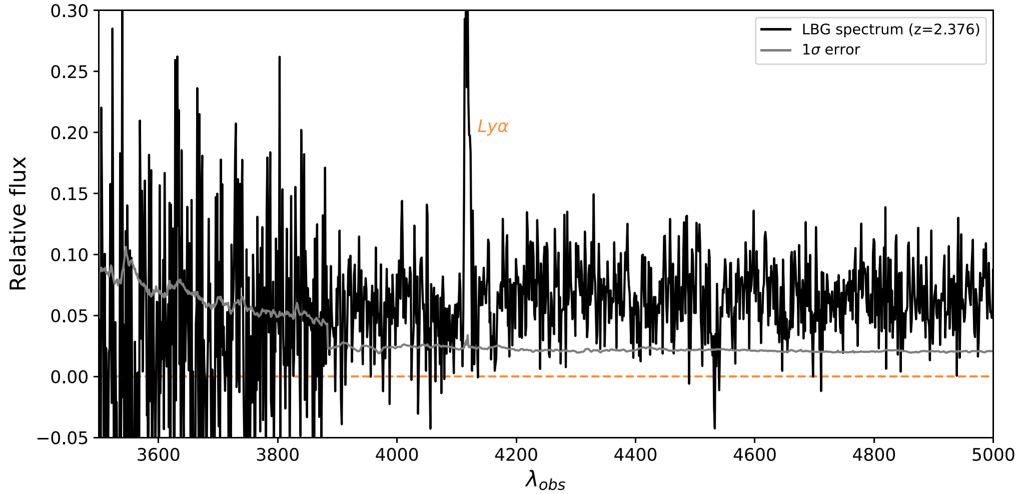

Figure 1. Example spectrum of a Lyman-break galaxy from the CLAMATO data release that fits our sample selection criteria. The spectrum shows a bright Lyα emission feature and weaker ISM features that are difficult to distinguish from the noise. An error spectrum (shown in gray) is reported with each source in the CLAMATO release.

$2.5 < z < 5.5$. Using only LBG spectra, they provided an assessment of $\tau_{\rm eff}$ without the systematic errors associated with normalizing quasar spectra.

In this work, we leverage the blue sensitivity of the Keck/LRIS spectrograph to measure $\tau_{\rm eff}$ from low signal-to-noise ratio (S/N) LBGs spectra at $z \lesssim 2.5$. Similarly, we set out to test previous work analyzing the effective opacity of the IGM by generating an estimate independent of the challenges associated with normalizing quasar spectra. Crucially, $z < 2.5$ is the regime where quasar measurements have traditionally been anchored on the grounds that one can more accurately estimate quasar continua at lower opacity.

In the following sections of this manuscript, we present the CLAMATO data sample (Section 2), describe our methodologies for creating composite spectra and fitting spectral energy distribution (SED) models (Section 3), report our measurements of $\tau_{\rm eff}$ and compare to previous studies (Section 4), and summarize and discuss this works findings (Section 5). Throughout the paper, we adopt a concordance Lambda cold-dark-matter (Λ-CDM) cosmology with $\Omega_\Lambda = 0.7$, $\Omega_m = 0.3$, and $h = 0.7$.

2. The CLAMATO Observations and Sample Selection

2.1. CLAMATO

Our sample of galaxies was drawn from the 2016 and 2017 releases of the CLAMATO, which were measured by the Low Resolution Imaging Spectrometer (LRIS) on the W.M. Keck I telescope (Oke et al. 1995). CLAMATO began operations in 2014 with the main goal of mapping the Lyα forest tomography of the foreground IGM (these pilot observations were not applicable to our analysis). Lee et al. (2014) found that because galaxies dominate the foreground UV luminosity function at faint magnitudes $g \sim 23$ (Reddy et al. 2008), LBG spectra would almost exclusively compose the 3D tomographic reconstruction.

CLAMATO is designed to systematically observe faint ($23 \lesssim g \lesssim 25$) UV-emitting sources from $2 < z < 3$, at high area densities ($\sim$1000 deg^2) and L18 report using a total of 240 background galaxies and QSOs within a 0.157 square degree section of the COSMOS field. They also report estimated redshift values and spectra on an additional 437 objects for a total of 677 reduced sources. The COSMOS field (Scoville et al. 2007) is in the Northern Hemisphere and spans 2 square degrees. It offers a large selection of g-band star-forming galaxies, covers a significant scale in the transverse direction ($\sim$10 Mpc), and has measurements of redshifts for the objects in the survey.

The target selection procedure for CLAMATO depends on the magnitude and probability of success, initial prioritization based on redshift, and the subsequent slit mask designs. As the COSMOS field has a rich selection of spectroscopic and multiwavelength imaging data, L18 built CLAMATO from existing redshift catalogs (Lilly et al. 2007; Kriek et al. 2015; Le Fevre 2015; Nanayakkara et al. 2016) that covered their desired wavelength range (3700 Å $< \lambda <$ 4300 Å). To select targets, L18 fed the combined spectroscopic and photometric catalogs to an algorithm that prioritizes background g-band sources in the redshift range of $2.25 \lesssim z \lesssim 2.45$. The algorithm prefers brighter sources due to slit-packing constraints but selects targets as faint as $g = 25.3$.

Observations for CLAMATO lasted a total of 15.5 nights, during which about 60 hr were spent on sky with a typical total exposure time per object lasting $\sim$9000 s. LRIS was configured with the 600/4000 grism to achieve an approximate resolution $R \equiv \lambda/\Delta\lambda \approx 1000$ with 1″ slits between the observer-frame wavelengths of 3700A and 4400A on its Blue channel. As expected with such faint and distant sources and an average seeing of 0.″7, the spectra have low signal-to-noise, S/N $<$ 3 per Å. The data were then processed using the LowRedux routines from the XIDL software package.[4] Figure 1 is an example of a reduced galaxy spectrum taken from the CLAMATO release described in L18.

L18 then assigned confidence ratings from 0 to 4 when estimating redshifts for each source, 0 being no attempt at all (normally reserved for corrupted data) and 4 being high confidence based on multiple lines. L18 reports that 66% of the objects in the sample had confidence ratings $\geqslant$3. The majority of less secure redshifts are for low priority sources used to fill spare slit space that often yielded spectra too noisy to identify.

4 http://www.ucolick.org/~xavier/LowRedux/

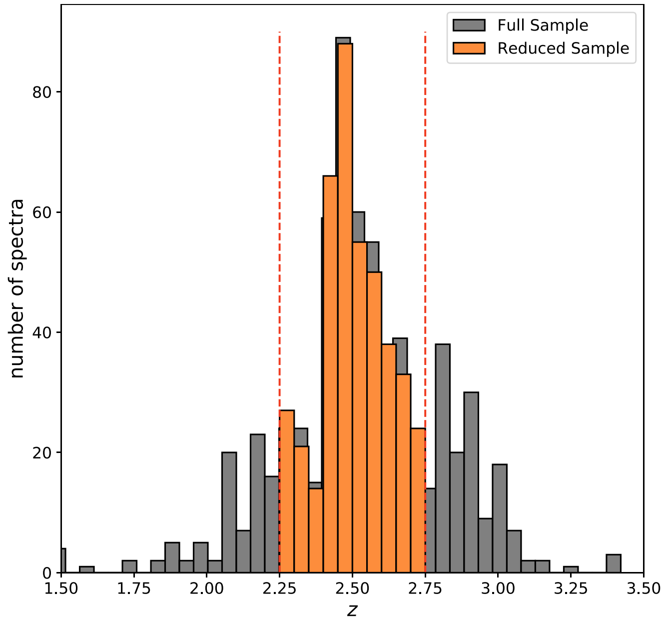

Figure 2. Redshift distribution of the complete CLAMATO sample (show in gray) vs. the reduced sample satisfying our selection criteria (shown in orange).

Approximately 95% of the objects with confidence ratings $\geqslant 3$, were identified as galaxies using LBG templates from Shapley et al. (2003), while the other 5%, were distinguished as broad-line quasars. For a more detailed outline of the selection algorithm, instrument specifications, and preliminary data reduction please see L18.

2.2. Sample Selection

Measuring the opacity, τ, from an individual object yields a single realization of the stochastic IGM. The effective opacity of the IGM τ_{eff} is the average estimated over many sight-lines. We measure τ_{eff} using a composite or "stacked" spectrum, which is essentially an average of flux values, at each wavelength. Alternatively, we could have measured the opacity from several different spectra, and then averaged, to yield τ_{eff}. There are two main justifications for why we chose to average our data before measuring the opacity. First, for small redshift variations, the observed continua of LBGs (or QSOs) are consistent across sight-lines, so a composite spectrum can be modeled by a single SED. Second, and more importantly, stacking improves the S/N allowing us to more accurately model the SED redward of Lyα.

To account for the fact that we are sampling the IGM with sight-lines corresponding to objects that are not at identical redshifts, we organize the CLAMATO spectra into small redshift bins of $\Delta z = 0.25$. This yields a median redshift z_{med}, which serves as a reference for the τ_{eff} values from the Lyα forest. In total, there are 566 CLAMATO galaxy spectra in the $2.0 \leqslant z \leqslant 3.0$ interval with the majority of these sources between $2.25 < z < 2.75$ (see Figure 2). We only used the $2.25 < z < 2.75$ interval because the bins to either side of it do not contain enough spectra to create an adequate stack. We split the majority interval into two redshift intervals: z_{low} from $2.25 < z < 2.50$ and z_{high} from $2.50 < z < 2.75$, for a combined total of 416 galaxy spectra.

Of our 416 galaxy spectra, several cover wavelengths blueward of the rest-frame Lyman limit (912 Å). For these spectra, we measure the median flux per pixel for wavelengths below the Lyman limit and exclude those with values outside of the ± 0.2 median flux interval (see Figure 3). We expect these spectra to have errors in their flux or sky subtraction, as a significant signal past the Lyman limit is highly improbable. We further cut down our sample by imposing a blanket S/N limit, using the mean flux value in the wavelength range of 1260–1304 Å. We found that a cutoff S/N = 1.5 excluded the poorest spectra without discarding the majority of the sample (see Figure 4). After these two cuts, we were left with 137 in

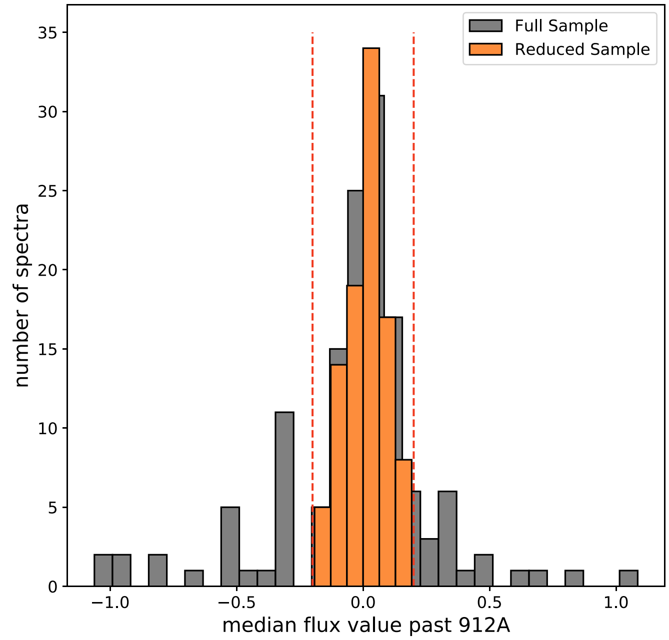

Figure 3. Complete distribution of median flux values taken from spectra that extend blueward of the Lyman limit (shown in gray). Those that are within the ± 0.2 cutoff (show in orange) are still considered viable. We cut our sample aggressively, excluding 49 spectra, so as to not skew the continuum blueward of $\sim$1130 Å.

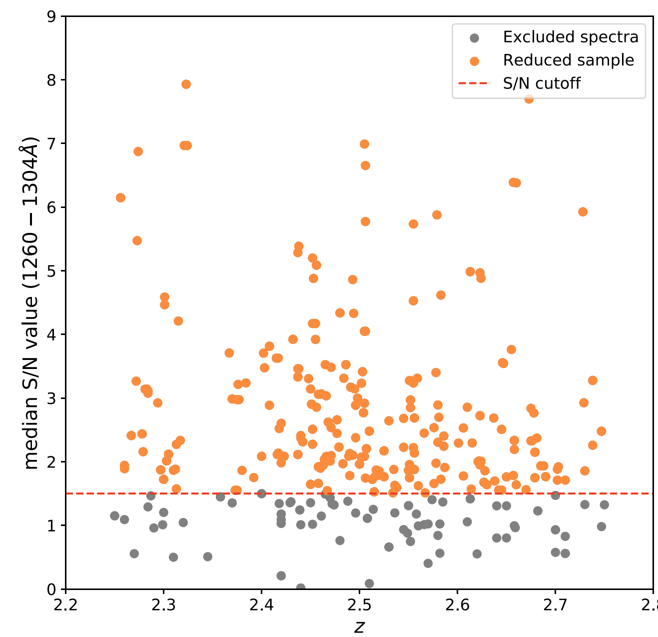

Figure 4. Scatter plot of our data's spectroscopic redshift vs. the S/N calculated in the 1260–1304 Å range for both the z_{low} and z_{high} intervals. The gray objects have been excluded by the S/N cut.

the z_{low} interval and 142 in the z_{high} interval for a combined total of 279 galaxy spectra. The z_{low} interval has a median redshift value of 2.43 and a standard deviation of 0.074. The z_{high} interval has a median redshift value of 2.58 and a standard deviation of 0.069. See Table A1 for the selected sample of galaxy spectra from the CLAMATO survey.

3. Composite Spectra

3.1. Stacking

The process that follows describes the preparation of individual LBG spectra prior to stacking:

1. To correct extinction from the Galactic interstellar medium (ISM), we passed each spectrum through a dereddening process based on the 3D Sky Map of Green et al. (2018). The Sky Map, given an object's coordinates, reports $E(B-V)$ extinction values for the Milky Way which we applied to the flux array using the the reddening curve from O'Donnell (1994; an updated version of Cardelli et al. 1989). No other corrections were necessary as the LRIS instrument has an atmospheric dispersion corrector and a fluxing term accounting for the atmospheric extinction.
2. We normalized the spectrum using values redward of Lyα, where there is no absorption features due to the IGM or ISM from 1260 to 1304 Å (between two Si II lines).
3. We trimmed the edges of the spectrum, only selecting flux data between $\lambda_{\mathrm{rest}} \approx 1050$–1400 Å.
4. We shifted the spectrum to the rest frame, using the redshift values measured by CLAMATO, and rebinned to a velocity dispersion of 300 km s^{-1} per pixel using a common starting wavelength of 1000 Å.

We then stacked the spectra by carrying out an unweighted, arithmetic mean of the flux values per wavelength. We chose not to weigh the spectra to better reduce cosmic variance in the Lyα forest (Becker et al. 2013). We averaged across 137 and 142 LBG spectra for the z_{low} and z_{high} intervals (respectively). The well behaved sections of the composites (1260–1304 Å, for example) were left with S/N values ∼30. The Lyα forest (1070–1170 Å), however, tended toward S/N values ∼10. Because, in general, all individual LBG spectra edges were quite noisy (see Figure 1) our stacks remained unconstrained blueward of ∼1040 and redward of ∼1400. See Figure 5 for the results of the stacking in black.

3.2. Bootstrapping

Our primary source of error comes from sample variance within the stack and not from the S/N values of each individual spectrum. To assess the error in τ_{eff}, we used a bootstrapping approach, following the example of Worseck et al. (2014). The following details our process for constructing a covariance matrix that assesses correlated errors in our τ_{eff} measurements in each redshift interval:

1. To estimate sample variance, we chose a random selection of LBG spectra, within each redshift interval (allowing for duplicates), equal to the number of spectra that comprised each original composite (137 for z_{low} and 142 for z_{high}).
2. We stacked the random selection in the same way as detailed above for creating the original composite.
3. We repeated the first two steps to generate 5000 randomized composites.
4. To normalize the randomized composites, we subtracted the original composite from each of them individually.
5. We compiled the randomized composites into an *IxJ* matrix (where $I = 5000$ and J is the length of our wavelength array (∼1000)) and dotted this matrix with its transpose to create a full covariance matrix. See Figure 5 for the the 1D diagonal results of the error analysis in gray.

3.3. SED Modeling

To measure τ_{eff}, we estimated the unabsorbed flux of the composites in the Lyα forest. Following the example of Paris et al. (2011), we extrapolated blueward of Lyα from a well behaved section of our spectra. We modeled the unabsorbed continua using an SED modeling technique designed by Chisholm et al. (2019; hereafter C19) to fit simple stellar population (SSPs) models from the Starburst99 (SB99) database (Leitherer et al. 1999). There are 50 SB99 single age, single metallicity stellar population models investigated in C19 where each model was created using a Kroupa initial mass function with a high-mass exponent of 2.3, a low-mass exponent of 1.3, and a high-mass cutoff of 100 $M_{\odot}$. As starlight between 1200 and 2000 Å is dominated by young massive O-stars (Leitherer et al. 1999), we only investigate a narrow regime of stellar ages: 1, 2, 3, 4, 5, 8, 10, 20, 40 Myr, each with five different metallicities: 0.05, 0.2, 0.4, 1.0, 2.0 $Z_{\odot}$. The FUV stellar continuum does not dramatically change for B-star dominated stellar populations between 40 and 200 Myr (de Mello et al. 2000; Rix et al. 2004), thus we use an upper age of 40 Myr. Each model is fully theoretical and does not include ISM lines. They were created by sampling the high-mass portion of the Hertzsprung–Russell diagram up to temperatures of 20,000 K and a high-mass cutoff of 100 $M_{\odot}$.

The modeling technique assumes that the spectra are combinations of multiple bursts of single age, single metallicity stellar populations and fits them with a uniform dust screen model dependent on four parameters: stellar attenuation ($E(B-V)$), the selected reddening curve (κ_{λ}), and linear coefficients (X_i) of each SB99 model (M_i) (see Equation (1) from C19). The stellar attenuation $E(B-V)$ is allowed to range from 0.0 to 5.0. C19 selects the reddening curve from Reddy et al. (2016) as it extends closer to the ionizing continua of massive stars (∼950 Å) than other models. C19 found that changing the attenuation law to that of Calzetti et al. (2000) reddens the inferred $E(B-V)$ by 0.01 mag.

The SED shape and observed stellar continuum can be fully described by these four parameters. Though the technique readily allows for more parameter constraints on the SED model, we did not define a free parameter for the absorption caused by the IGM (τ_{eff}). To do so, we would have had to subscribe to a predetermined functional form for the redshift evolution of τ_{eff}. Instead, we explored the results independent of any such formalism.

Using MPFIT (Markwardt 2009), an IDL-based, least-squares fitting package,[5] we determined the linear combination

[5] https://pages.physics.wisc.edu/~craigm/idl/fitting.html

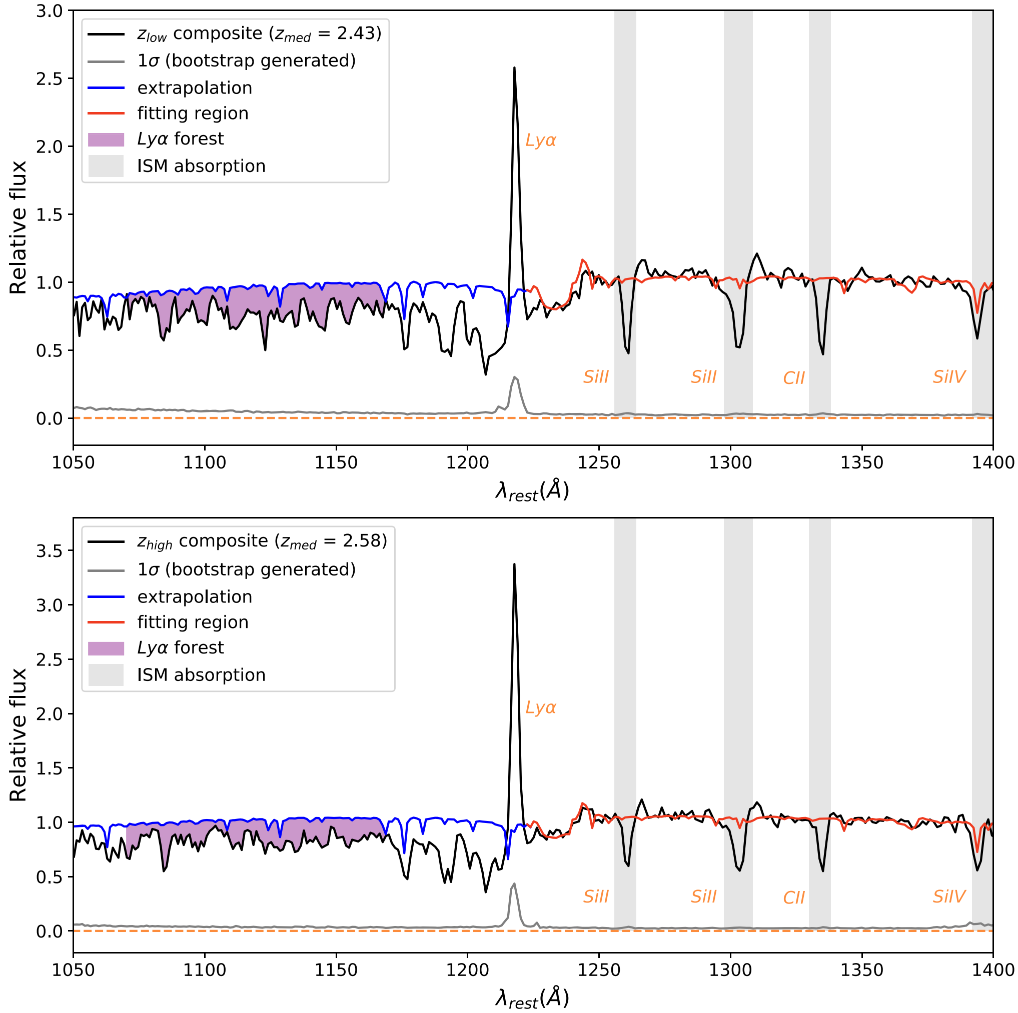

Figure 5. Unshuffled $z_{\rm low}$ and $z_{\rm high}$ composite spectra and their SED fits. The SED fits are two-toned, showing the region in which the fit is constrained by our data (red) and where the fit is extrapolated to measure the forest (blue). The excess flux in the model, blueward of Lyα, is caused by H I attenuation by the IGM. The error spectrum is based on the bootstrap matrix (plotted in gray; see Section 3.2). Some of the most prominent ISM transitions are denoted in gray and were not included in the fit.

of coefficients ($X_i \geqslant 0$) that best describe the observed stellar continuum. The linear coefficients can also be translated to light fractions ($L_{\rm frac}$) that each model M_i contributes to the total intrinsic flux at 1270 Å. Using these light fractions, we can estimate the age and the metallicity of the source (see Table 2). These light-weighted properties of our SSPs are driven by spectral features that are less degenerate than the spectral shape alone. C19 explores the stability of the fitting procedure by measuring the change in flux (per wavelength index) for variations in metallicity and age of model M_i. Increasing the age of a 0.2 $Z_\odot$ model from 2 to 8 Myr, changed the integrated root square flux of the SED by 2.4 in the 1250–1350 Å region. Increasing the metallicity of a 5 Myr model from 0.05$Z_\odot$ to 0.4$Z_\odot$, changed the integrated root square flux of the SED by 2.1 in the same wavelength region.

The following procedure was used to apply the C19 SED modeling technique to our two LBG composites and 10,000 randomized iterations (we used the 1D error spectra defined in Section 3.2 for each redshift bin accordingly):

1. We masked out 14 ISM absorption lines and nonresonant emissions ($\pm$500 km s^{-1}) redward of Lyα that would otherwise contaminate the fitting (see Table 1).

Table 1
The Transition Lines between ∼1230 and 1400 Å Excluded from Our SB99 Fitting

Ion	$\lambda_{\rm lab}$ (Å)
H I	1215.67
N V	1238.82
N V	1242.80
Si II	1260.42
Si III	1294.54
C III	1296.33
Si III	1296.74
Si III	1298.93
O I	1302.17
Si II	1304.37
Ni II	1317.22
C II	1334.53
C II’	1335.71
Si IV	1393.76
Si IV	1402.77

Note. Most of these ions are from the ISM (Leitherer et al. 2011) and were masked so that the fit could be extended blueward of Lyα. Each line was padded with a $\pm$500 km s^{-1} buffer.

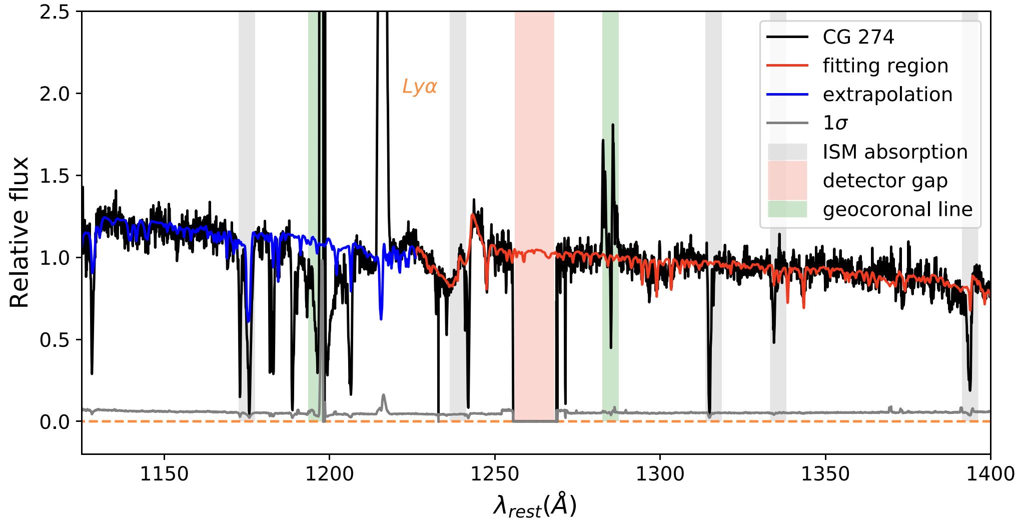

Figure 6. Example of the C19 SB99 fitting routine successfully modeling the continuum shape blueward of Lyα. CG 274 was normalized at 1270 Å and was fit in the 1223–1406 Å region. The SED model extends to $\sim$1100 Å. There are two Earth-glow sky emission features (shown in green) at 1195 and 1290 Å several ISM absorption lines that are not part of the actual galaxy spectrum. Figure 2 from Chisholm et al. (2015) also demonstrates similar success at reproducing the blue continuum.

Table 2
Best-fit Parameters and Derived Values from the SB99 SED Modeling for Our Two Composites

Redshift Interval	$N_{\rm spec}$	χ^2	$E(B-V)$	Age (Myr)	Metallicity ($Z_\odot$)
2.43 ($z_{\rm low}$)	137	4.048	0.261	6.8	0.05
2.58 ($z_{\rm high}$)	142	2.345	0.235	5.0	0.05

2. We fit our data in the 1225–1400 Å range, to take advantage of the unattenuated sections of our spectra and extrapolate the continuum into the Lyα forest.
3. Using the attenuation curve from Reddy et al. (2016), we reddened our fitting results and normalized them in the same range as the composites (1260–1304 Å).
4. We rebinned the SED models to a matching velocity dispersion of 300 km s^{-1}. See Table 2 for the fitted parameters. In the end we were left with the unabsorbed continua of our two composites and those of the 10,000 bootstrap iterations.

To demonstrate the stability of our selected fitting technique, we include the fitted SED of a low-z galaxy, CG 274, which has negligible attenuation by the IGM (see Figure 6). This spectrum was taken by the Cosmic Origins Spectrograph on the Hubble Space Telescope using the G130M grating and a central wavelength of 1291 Å (Program ID: 15099; PI: Chisholm). At a redshift $z = 0.0148$, it does not exhibit any notable Lyα forest absorption. We modeled its flux redward of Lyα in a similar fashion to the $z \sim 2$ composites and then extrapolated blueward. We find that the extrapolation accurately reproduces the stellar continuum shape, validating our procedure.

4. $\tau_{\rm eff}$ Measurements and Associated Errors

Armed with an SED model for each composite and bootstrap realization, we analyzed the Lyα forest to measure an effective opacity at each wavelength index. We used the 1070–1170 Å range to avoid continuum fitting problems associated with rapidly changing emission-line profiles, and possible contamination from the proximity effect (Kirkman et al. 2005). For each stack, we masked the following forest ISM lines with a $\pm$ 5 Å buffer: 1083.99, 1117.97, 1122.52, 1128.01, 1144.93, 1152.81 Å. Next, we measured the effective opacity of every stack/model pair for each wavelength index.

$$\tau_{\rm eff} = -\ln \frac{F_{\rm obs}}{F_{\rm model}}. \quad (1)$$

Here, $F_{\rm obs}$ is the average flux and $F_{\rm model}$ is the extrapolated SED.

4.1. Metal Corrections

As we hoped to compare our $\tau_{\rm eff}$ directly to other works that carry out similar analyses (Schaye et al. 2003; Kirkman et al. 2005; Becker et al. 2013), we corrected our values for absorption from metal lines. Though there are several ways of addressing the contribution to $\tau_{\rm eff}$ from metal absorption (or damped absorbers in the case of quasar spectra) we followed the example of Kirkman et al. (2005) by subtracting the metal absorption statistically. We chose to apply this method because their solution did not require identification of contaminating metal lines by eye like that of Schaye et al. (2003). Instead Kirkman et al. (2005) built upon a method originally designed by Tytler et al. (2004) and estimated the metal absorption over the extended redshift range (1.7–3.54) using a sample of 52 quasars.

In general the absorption due to metals in composite spectra essentially scales the mean flux by a relatively minor factor, which becomes increasingly less important at higher redshifts ($z \sim 4$) (Becker et al. 2013). In fact Faucher-Giguere et al. (2008) compared the two correction methods from Schaye et al. (2003) and Kirkman et al. (2005), finding that either method was accurate to the level of their statistical error bars.

To find the metal contribution as a function of rest-frame wavelength, we used Kirkman et al. (2005), Equation (1). They define DM as the amount of absorption from metal lines alone, as originally coined in Tytler et al. (2004). We converted the

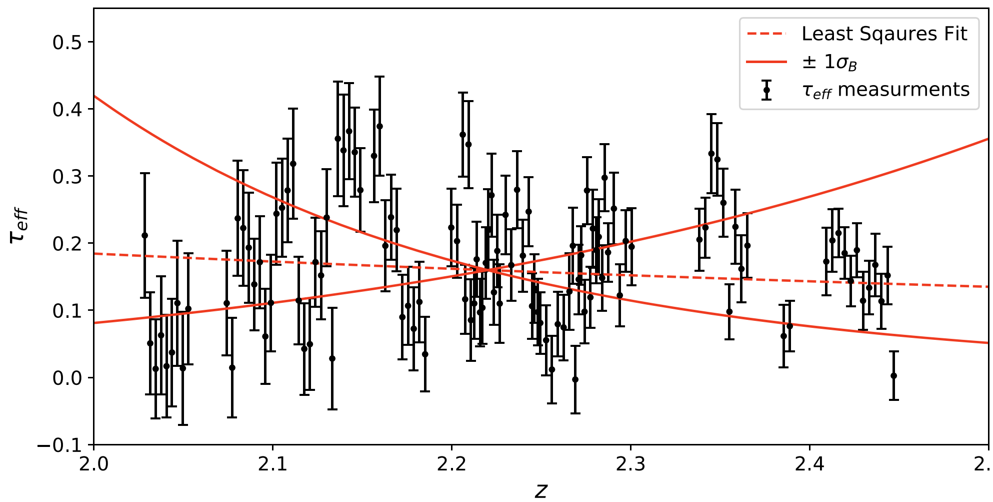

Figure 7. Our measurements of τ_{eff} as a function of redshift from both redshift intervals. Though we used the full covariance matrix to fit our data with the power law from Equation (6), only the diagonals of the matrix are shown. The best fit is plotted by the dotted line with a 1σ uncertainty in the power-law exponent plotted as solid lines.

DM value to τ_M despite the fact that DM is approximately equal to τ_M for z ~2.

$$\mathrm{DM} = 0.0156 - (4.646 * 10^{-5})(\lambda_{\mathrm{rest}} - 1360\ \text{Å}) \tag{2}$$

$$\tau_M = \ln(1 + \mathrm{DM}). \tag{3}$$

Where τ_M is the contribution to the absorption from metals and where λ_{rest} is a wavelength index in the forest of the stack. Then, by subtracting the contribution from metals we were left with corrected values of τ_{eff}.

$$\tau_{\mathrm{eff}} = \tau_{\mathrm{total}} - \tau_M. \tag{4}$$

Where τ_{total} is simply the total observed optical depth and τ_{eff} is the observed optical depth that has been corrected for metal absorption.

4.2. Redshift Interval

Finally, because we were interested in measuring the redshift evolution of τ_{eff} we converted the wavelength arrays to values of z, sampling the entirety of the redshift window included in each stack.

$$z_i = (\lambda_{\mathrm{rest}}/1216\ \text{Å})(1 + z_{\mathrm{med}}) - 1, \tag{5}$$

where z_i is the redshift of a particular absorber in the IGM and z_{med} is the median redshift value of each stack. Because the z_{med} values of our two composite intervals were similar, their redshift coverage overlapped (see Table A2). Combining both redshift intervals, we were left with a total of 88 indices (56 from the z_{high} interval and 58 from the z_{low} interval) from which we measured τ_{eff} in the 1070–1170 Å range. This combined redshift sample extended from 2.02 to 2.44, with a median value of 2.22.

4.3. Error Estimates on τ_{eff}

The errors on the τ_{eff} values (σ_τ) were directly measured from the bootstrap analysis but were not simply the standard deviation of each redshift interval across the bootstrap. Instead, we report the diagonals of the covariance matrices in τ_{eff}(found using the same method as described in Section 3.2). We did not report uncertainty for redshift values as they were only dependent on the z_{med} and λ_i, neither of which had defined errors. For our combined set of measurements and their 1D errors, see Table A2.

4.4. Power-law Fitting

Using a least-squares formalism and the full bootstrap-generated covariance matrices, we fit our combined measurements of τ_{eff} with the following analytic power-law function.

$$\tau_{\mathrm{eff}} = A[(1 + z)/(1 + z_{\mathrm{piv}})]^B, \tag{6}$$

where A and B are the scale factor and power-law index parameters. The z_{piv} value included in the fitting function, shifts the power-law index pivot, normalizing the fit to our redshift range (Becker et al. 2013). We chose $z_{\mathrm{piv}} = 2.22$ as it is the median value of our Lyα forest redshift distribution as measured from 5. Our best-fit scale factor and power-law index parameters are $A = 0.159 \pm 0.001$ and $B = -2.022 \pm 11.60$ respectively. As shown in Figure 7, the measurements scatter about this curve in a roughly stochastic manner consistent with the uncertainty estimates. One does, however, identify a set of measurements that lie significantly above the model at $z \sim 2.1$–2.2. We attribute these fluctuations to spectral features not smoothed out in our composite spectra. They have not greatly influenced the model because of their small number and significant error estimates.

4.5. Redshift Evolution in τ_{eff}

With a best-fit power-law index error σ_B=11.60, we report poor sensitivity to the known evolution of τ_{eff} at redshifts higher than $z = z_{\mathrm{piv}}$. In short, the redshift evolution of τ_{eff} past $z \sim 3$ was difficult to model given the scatter of our measurements in our narrow redshift window $\Delta z \sim 0.5$ (see Figure 7).

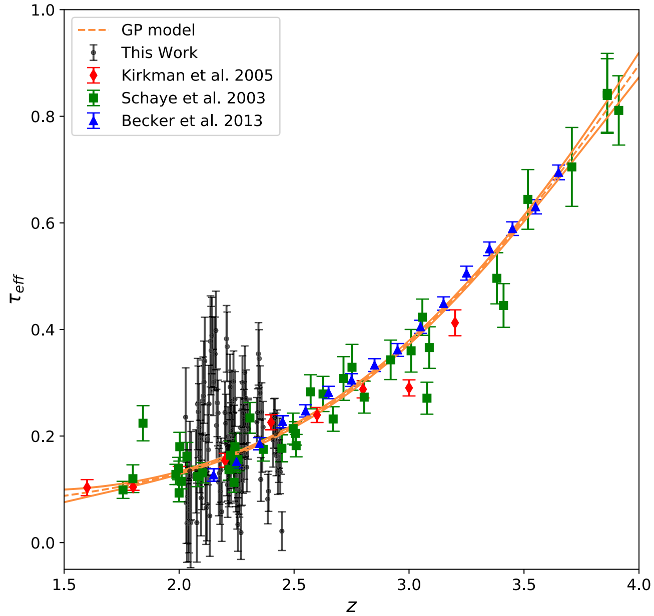

Figure 8. Best-fit GP model and associated uncertainty. All of the data points included in the figure (Schaye et al. 2003; Kirkman et al. 2005; Becker et al. 2013) were corrected for intervening metals (and optically thick absorbers in the case of the QSO studies). All analyses shown were used to constrain the GP model, which successfully predicts the steep redshift evolution in $\tau_{\rm eff}$.

Evaluating our model at $z = z_{\rm piv}$ we found $\tau_{\rm eff} = 0.159 \pm 0.001$. This uncertainty does not include a contribution from the error in our power-law index parameter. We excluded σ_B in our error estimate at $z = z_{\rm piv}$ because our data were not sensitive to that parameter. We note that our statistical estimate in the uncertainty of $\tau_{\rm eff}$ at $z = z_{\rm piv}$ ignores systematic errors, which we expect to be at least 10%.

Comparing our linear fit's prediction of $\tau_{\rm eff}$ at $z = z_{\rm piv}$ to previous estimates from analysis of quasar spectra; Kirkman et al. (2005) and Becker et al. (2013) $\tau_{\rm eff} = 0.143, 0.152$ (respectively), we found good agreement. We did not find similar compliance with the power-law fit from Schaye et al. (2003) as they predicted $\tau_{\rm eff} = 0.298$ at $z = z_{\rm piv}$. This might be because their sample of 21 quasars was significantly contaminated by metal lines, resulting in slight overestimation around $z \sim 2$.

To further compare results against previous works (Schaye et al. 2003; Kirkman et al. 2005; Becker et al. 2013) and to model the redshift evolution of $\tau_{\rm eff}$ past $z \sim 3$, we looked to Gaussian processes (GP). While common practice is to fit such data with a power law (Equation (6)), recent data sets are not sufficiently well-described by this model (Becker et al. 2013). Therefore, we analyzed our data alongside the results from Schaye et al. (2003), Kirkman et al. (2005), and Becker et al. (2013) with a GP model that solves for the optimal functional form describing the data. After experimentation, we settled on a radial basis function kernel that has mean-square derivatives of all orders and thus creates a smooth fit (see Figure 8). This model is provided by the SciKit Learn toolbox.[6] We did not fit the GP model with our full covariance matrix, nor did we use any of the reported 2D errors (Schaye et al. 2003; Kirkman et al. 2005; Becker et al. 2013). Instead, to simplify the analyses, we only used the 1D diagonals as errors in our measurement.

[6] https://scikit-learn.org/stable/modules/generated/sklearn.gaussian_process.kernels.RBF.html

5. Summary and Concluding Remarks

We used 281 LBG spectra collected by the CLAMATO survey to create two composite spectra in the following redshift intervals: $2.25 < z < 2.5$ and $2.5 < z < 2.75$. The normalized composites were fit with SSP SB99 models at rest wavelengths 1225–1400 Å. Extrapolations of these models blueward of Lyα provided estimates of the effective optical depth $\tau_{\rm eff}$ of the IGM from $z \approx 2.0$–2.5. We derived bootstrap-generated errors based on the variance in our LBG stacking and propagated these through to the SED fitting.

Our primary results are:

1. A best-fit to the power law $\tau_{\rm eff} = A[(1 + z)/(1 + 2.22)]^B$, giving measurements $A = 0.159 \pm 0.001$ and $B = -2.022 \pm 11.60$.
2. Our estimate of $\tau_{\rm eff}$=0.159 ± 0.001 at $z = 2.22$ is in good agreement with previous estimations based on quasar analysis. This demonstrates that quasar continuum estimations at $z < 2.5$ are not subject to large systematic uncertainties.
3. A GPs prediction of the redshift evolution of $\tau_{\rm eff}$ using a radial basis kernel. In conjunction with Schaye et al. (2003), Kirkman et al. (2005), and Becker et al. (2013) we show strong evolution in $\tau_{\rm eff}$ at $z > 2$.

As we progress to the next generation of large-scale galaxy surveys at $z > 2$ (e.g., the Prime Focus Spectrograph survey), it is possible that measurements of $\tau_{\rm eff}$ will be drawn primarily from analyses of LBGs. Of course, a continued comparison between quasars and galaxies will be critical to assess systematic uncertainties associated with continuum estimation.

We thank the anonymous referee for a careful reading of the original manuscript and insightful suggestions. J.M. would like to thank Marie Lau, Sunil Sihma, and Jiani Ding for their input with several aspects of this project. K.G.L. acknowledges support from JSPS KAKENHI Grant Number JP19K14755. The data presented herein were obtained at the W.M. Keck Observatory, which is operated as a scientific partnership among the California Institute of Technology, the University of California and the National Aeronautics and Space Administration (NASA). The Observatory was made possible by the generous financial support of the W.M. Keck Foundation. The authors also wish to recognize and acknowledge the very significant cultural role and reverence that the summit of Maunakea has always had within the indigenous Hawai'ian community. We are most fortunate to have the opportunity to conduct observations from this mountain. Support for this work was provided by NASA through the NASA Hubble Fellowship grant #51432 awarded by the Space Telescope Science Institute, which is operated by the Association of Universities for Research in Astronomy, Inc., for NASA, under contract NAS5-26555. Based on observations made with the NASA/ESA Hubble Space Telescope, obtained from the data archive at the Space Telescope Science Institute. STScI is operated by the Association of Universities for Research in Astronomy, Inc., under NASA contract NAS 5–26555. Support for this work was provided by NASA through grant number 15099 from the Space Telescope Science Institute, which is operated by AURA, Inc., under NASA contract NAS 5–26555.

Appendix

Table A1
The Sample of CLAMATO LBGs Used in Our Composite Analysis

CLAMATO ID	R.A.	Decl.	z
cl2016comb-zsp2.3-00871	150.08844	2.24847	2.301
cl2016comb-zsp2.6-00923	150.0679	2.15819	2.621
cl2016comb-zsp2.5-00941	150.03569	2.2896	2.45
cl2016comb-zsp2.7-00954	150.02919	2.25323	2.66
cl2016comb-zsp2.4-01012	150.05318	2.1513	2.516
cl2016comb-zsp2.6-01016	150.02277	2.14595	2.624
cl2016comb-zsp2.4-01321	150.02322	2.37721	2.384
cl2016comb-zsp2.7-01349	150.0231	2.31791	2.675
cl2016comb-zsp2.6-01865	150.1011	2.24173	2.647
cl2016comb-zph2.5-12541	150.10332	2.2585	2.438
cl2016comb-zph2.6-12722	150.09888	2.16134	2.416
cl2016comb-zph2.3-12836	150.04671	2.25102	2.284
cl2016comb-zph2.6-15035	150.09714	2.45167	2.479
cl2016comb-zph2.4-15059	150.16531	2.42249	2.506
cl2016comb-zph2.3-15171	150.09419	2.34853	2.273
cl2016comb-zph2.6-15218	150.17313	2.3254	2.613
cl2016comb-zsp2.6-15363	149.98645	2.37884	2.545
cl2016comb-zsp2.4-15373	150.00044	2.37243	2.42
cl2016comb-zph2.4-15473	150.04306	2.31694	2.44
pc06-zph2.3-15159	150.09453	2.35827	2.466
pc06-zsp2.4-00852	150.06163	2.28314	2.377
cpilot06-zsp2.7-00857	150.09343	2.27371	2.65
cpilot06-zsp2.7-01260	150.07938	2.3406	2.679
cpilot06-zsp2.7-01276	150.0798	2.30685	2.679
cpilot06-zsp2.7-01324	150.03629	2.37356	2.73
cpilot05-zph2.3-12714	150.0827	2.16487	2.26
cpilot02-zph2.5-12826	150.00772	2.24664	2.525
cpilot02-zph2.5-12988	149.98288	2.1657	2.42
cpilot02-zsp2.3-00962	150.00296	2.24145	2.267
cpilot02-zsp2.3-01013	149.96033	2.15784	2.297
cpilot02-zsp2.4-00965	149.99504	2.2398	2.442
cpilot02-zsp2.4-01882	149.99516	2.23734	2.45
cpilot02-zsp2.5-00990	149.98834	2.20705	2.458
cpilot02-zsp2.6-00986	149.99481	2.21234	2.556
cpilot02-zsp2.6-01009	150.0136	2.16877	2.623
cpilot02-zsp2.7-00982	150.02107	2.21256	2.658
cpilot09-zph2.5-15182	150.12419	2.34884	2.513
cpilot09-zph2.5-15268	150.15688	2.30079	2.505
cpilot09-zph2.6-12505	150.21675	2.36974	2.408
cpilot09-zph2.6-15214	150.11501	2.3276	2.551
cpilot09-zph2.7-15220	150.12335	2.32413	2.623
cpilot09-zsp2.5-00856	150.161	2.2759	2.504
cpilot09-zsp2.5-01753	150.15979	2.37123	2.458
cpilot09-zsp2.5-01754	150.14763	2.36719	2.452
cpilot09-zsp2.6-01252	150.16002	2.35477	2.556
cpilot09-zsp2.6-01262	150.11871	2.33762	2.552
cpilot09-zsp2.7-00858	150.14117	2.27234	2.747
cpilot08-zph2.2-12568	150.16913	2.23838	2.451
cpilot08-zph2.3-01886	150.21675	2.36974	2.305
cpilot08-zph2.5-12604	150.1651	2.22747	2.437
cpilot08-zsp2.3-00892	150.10474	2.21573	2.324
cpilot08-zsp2.4-00877	150.12111	2.23542	2.432
cpilot08-zsp2.7-00889	150.14442	2.21977	2.702
cpilot08-zsp2.7-00903	150.1205	2.1923	2.688
cpilot08-zsp2.7-00933	150.10455	2.13738	2.69
cpilot03-zph2.4-15492	149.95932	2.30758	2.555
cpilot03-zph2.6-12812	150.0199	2.26976	2.42
cpilot03-zsp2.3-01330	149.99364	2.36083	2.256
cpilot03-zsp2.5-01345	150.0118	2.32297	2.467
cpilot03-zsp2.6-01352	150.01968	2.31087	2.624
cpilot12-zph2.4-14888	150.24263	2.35848	2.278
cpilot12-zph2.4-14925	150.23189	2.33713	2.456
cpilot12-zph2.4-15146	150.22118	2.37094	2.52

Table A1
(Continued)

CLAMATO ID	R.A.	Decl.	z
cpilot12-zph2.6-12247	150.24257	2.27782	2.525
cpilot12-zph2.6-14947	150.2346	2.33237	2.505
cpilot12-zph2.6-15161	150.22186	2.36248	2.5
cpilot12-zph2.6-15173	150.22505	2.35619	2.507
cpilot12-zsp2.5-01268	150.21138	2.32292	2.46
cpilot12-zsp2.5-01274	150.22343	2.3072	2.491
cpilot12-zsp2.7-01272	150.19978	2.3155	2.738
npc05-zph2.3-12595	150.07341	2.23328	2.303
npc05-zph2.3-12701	150.07675	2.17348	2.486
npc05-zph2.5-12653	150.06866	2.18897	2.3
npc05-zsp2.3-00964	150.05905	2.24059	2.283
npc05-zsp2.4-01861	150.08061	2.24284	2.437
c16-24-zph2.4-15103	150.22504	2.39841	2.645
c16-24-zph2.4-15121	150.2166	2.37826	2.373
c16-24-zph2.6-17723	150.21797	2.49178	2.645
c16-24-zph2.7-17497	150.22946	2.47711	2.66
c16-24-zsp2.5-01778	150.19771	2.48577	2.49
c16-24-zsp2.6-01219	150.20456	2.45545	2.58
c16-24-zsp2.7-01779	150.20668	2.48269	2.676
c16-11-zph2.4-12707	150.20447	2.17102	2.37
c16-11-zph2.5-12304	150.22772	2.23602	2.493
c16-11-zph2.5-12634	150.18759	2.20976	2.48
c16-11-zsp2.3-00873	150.19859	2.24642	2.367
c16-11-zsp2.4-00884	150.20885	2.22566	2.437
c16-11-zsp2.5-00834	150.23257	2.14658	2.638
c16-20-zph2.6-17715	150.09602	2.49511	2.536
c16-20-zph2.6-26486	150.06027	2.3877	2.55
c16-20-zsp2.5-01241	150.07576	2.38064	2.466
c16-20-zsp2.7-01233	150.08762	2.39438	2.702
c16-22-zph2.4-15040	150.13757	2.44066	2.51
c16-22-zph2.6-17758	150.10231	2.47219	2.606
c16-22-zsp2.5-01239	150.14885	2.38391	2.505
c16-18-zph2.6-15288	149.95987	2.45353	2.515
c16-18-zph2.6-15292	149.95877	2.45022	2.627
c16-18-zsp2.4-01589	150.01366	2.46674	2.417
cl2017comb-zsp2.5-00834	150.23257	2.14658	2.637
cl2017comb-zsp2.3-00871	150.08844	2.24847	2.301
cl2017comb-zsp2.6-00923	150.0679	2.15819	2.622
cl2017comb-zsp2.7-00954	150.02919	2.25323	2.657
cl2017comb-zsp2.6-00966	150.03355	2.23549	2.555
cl2017comb-zsp2.4-01003	150.05382	2.185	2.56
cl2017comb-zsp2.4-01012	150.05318	2.1513	2.452
cl2017comb-zsp2.6-01016	150.02277	2.14595	2.623
cl2017comb-zsp2.3-01181	150.33495	2.36654	2.315
cl2017comb-zsp2.5-01239	150.14885	2.38391	2.507
cl2017comb-zsp2.5-01245	150.1015	2.37672	2.464
cl2017comb-zsp2.4-01265	150.06456	2.32904	2.447
cl2017comb-zsp2.4-01321	150.02322	2.37721	2.376
cl2017comb-zsp2.7-01349	150.0231	2.31791	2.678
cl2017comb-zsp2.6-01865	150.1011	2.24173	2.646
cl2017comb-zph2.5-12541	150.10333	2.25851	2.437
cl2017comb-zph2.6-12722	150.09888	2.16134	2.417
cl2017comb-zsp2.3-12836	150.04671	2.25102	2.284
cl2017comb-zph2.5-14852	150.3867	2.37505	2.456
cl2017comb-zph2.6-15035	150.09714	2.45167	2.479
cl2017comb-zsp2.5-15059	150.16531	2.42249	2.506
cl2017comb-zph2.3-15171	150.09421	2.34853	2.274
cl2017comb-zph2.6-15218	150.17313	2.3254	2.613
cl2017comb-zsp2.4-15373	150.00044	2.37243	2.418
cl2017comb-zph2.7-15399	150.0201	2.35363	2.689
cl2017comb-zph2.4-15473	150.04306	2.31694	2.44
cl2017comb-zsp2.6-15492	149.95932	2.30758	2.555
cl2017comb-zsp2.6-17758	150.10231	2.47219	2.606

Table A1
(Continued)

CLAMATO ID	R.A.	Decl.	z
pc06-zph2.3-15159	150.09453	2.35827	2.461
pc06-zsp2.4-00852	150.06163	2.28314	2.375
cpilot06-zsp2.7-00857	150.09343	2.27371	2.65
cpilot06-zsp2.7-01260	150.07938	2.3406	2.679
cpilot06-zsp2.7-01276	150.0798	2.30685	2.679
cpilot05-zph2.3-12714	150.0827	2.16487	2.26
cpilot05-zsp2.7-00994	150.04597	2.20114	2.709
cpilot02-zph2.5-12826	150.00772	2.24664	2.525
cpilot02-zph2.5-12988	149.98288	2.1657	2.42
cpilot02-zsp2.3-00962	150.00296	2.24145	2.267
cpilot02-zsp2.3-01013	149.96033	2.15784	2.297
cpilot02-zsp2.4-00965	149.99504	2.2398	2.442
cpilot02-zsp2.4-01882	149.99516	2.23734	2.45
cpilot02-zsp2.5-00990	149.98834	2.20705	2.458
cpilot02-zsp2.6-00986	149.99481	2.21234	2.556
cpilot02-zsp2.6-01009	150.0136	2.16877	2.623
cpilot02-zsp2.7-00982	150.02107	2.21256	2.658
cpilot09-zph2.5-15182	150.12419	2.34884	2.513
cpilot09-zph2.5-15268	150.15688	2.30079	2.502
cpilot09-zph2.6-12505	150.14354	2.28177	2.408
cpilot09-zph2.6-15214	150.11501	2.3276	2.552
cpilot09-zph2.7-15220	150.12335	2.32413	2.623
cpilot09-zsp2.5-00856	150.161	2.2759	2.504
cpilot09-zsp2.5-01753	150.15979	2.37123	2.46
cpilot09-zsp2.5-01754	150.14763	2.36719	2.455
cpilot09-zsp2.6-01252	150.16002	2.35477	2.556
cpilot09-zsp2.6-01262	150.11871	2.33762	2.552
cpilot09-zsp2.7-00858	150.14117	2.27234	2.747
cpilot08-zph2.2-12568	150.16913	2.23838	2.451
cpilot08-zph2.3-01886	150.12947	2.2072	2.305
cpilot08-zph2.5-12604	150.1651	2.22747	2.437
cpilot08-zsp2.3-00892	150.10474	2.21573	2.321
cpilot08-zsp2.4-00877	150.12111	2.23543	2.432
cpilot08-zsp2.7-00889	150.14442	2.21977	2.71
cpilot08-zsp2.7-00903	150.1205	2.1923	2.685
cpilot08-zsp2.7-00933	150.10455	2.13738	2.69
cpilot03-zsp2.3-01330	149.99364	2.36083	2.256
cpilot03-zsp2.7-00951	150.0182	2.25944	2.673
cpilot12-zph2.4-14888	150.24263	2.35848	2.278
cpilot12-zph2.4-14925	150.23189	2.33713	2.456
cpilot12-zph2.4-15146	150.22118	2.37094	2.517
cpilot12-zph2.6-12247	150.24257	2.27782	2.525
cpilot12-zph2.6-14947	150.2346	2.33237	2.505
cpilot12-zph2.6-15161	150.22186	2.36248	2.5
cpilot12-zph2.6-15173	150.22505	2.35619	2.507
cpilot12-zsp2.5-01268	150.21138	2.32292	2.46
cpilot12-zsp2.5-01274	150.22343	2.3072	2.491
cpilot12-zsp2.5-01678	150.22528	2.3512	2.484
cpilot12-zsp2.7-01272	150.19978	2.3155	2.738
npc05-zph2.3-12595	150.07341	2.23328	2.303
npc05-zph2.3-12701	150.07675	2.17348	2.486
npc05-zph2.5-12653	150.06866	2.18897	2.3
npc05-zsp2.3-00964	150.05905	2.24059	2.281
npc05-zsp2.4-01861	150.08061	2.24284	2.437
c16-24-zph2.4-15103	150.22504	2.39841	2.642
c16-24-zph2.4-15121	150.2166	2.37826	2.375
c16-24-zph2.6-17723	150.21797	2.49178	2.645
c16-24-zph2.7-17497	150.22946	2.47711	2.628
c16-24-zsp2.5-01778	150.19771	2.48577	2.535
c16-24-zsp2.6-01219	150.20456	2.45545	2.586
c16-24-zsp2.7-01779	150.20668	2.48269	2.675
c16-11-zph2.3-12434	150.23575	2.1661	2.31
c16-11-zph2.3-12690	150.21985	2.17724	2.61
c16-11-zph2.4-12707	150.20447	2.17102	2.37
c16-11-zph2.5-12304	150.22772	2.23602	2.489
c16-11-zph2.5-12634	150.18759	2.20976	2.48
c16-11-zsp2.4-00884	150.20885	2.22566	2.438
c16-20-zph2.6-17715	150.09602	2.49511	2.538
c16-20-zph2.6-26486	150.06027	2.3877	2.55
c16-20-zsp2.5-01241	150.07576	2.38064	2.469
c16-20-zsp2.7-01233	150.08762	2.39438	2.703
c16-22-zph2.4-15040	150.13757	2.44066	2.51
c16-18-zph2.6-15288	149.95987	2.45353	2.515
c16-18-zph2.6-15292	149.95877	2.45022	2.627
c16-18-zsp2.4-01589	150.01366	2.46674	2.415
c16-18-zsp2.5-01298	149.97008	2.43493	2.458
c17-27s-zph2.4-12455	150.24768	2.15066	2.294
c17-27s-zph2.5-12355	150.25565	2.21225	2.578
c17-27s-zph2.5-32293	150.2847	2.21318	2.503
c17-27s-zph2.6-12374	150.27167	2.20637	2.615
c17-27s-zph2.7-12405	150.27063	2.18604	2.58
c17-27s-zph2.7-32286	150.27771	2.21997	2.495
c17-27s-zsp2.3-00805	150.30594	2.19577	2.323
c17-27s-zsp2.5-00785	150.27141	2.24478	2.506
c17-27s-zsp2.6-00783	150.28088	2.24953	2.579
c17-27s-zsp2.6-00793	150.27214	2.2301	2.611
c17-27s-zsp2.6-00823	150.26257	2.16603	2.601
c17-28s-zph2.6-12252	150.30026	2.27421	2.581
c17-28s-zph2.6-14978	150.29825	2.31653	2.576
c17-28s-zsp2.4-01216	150.26845	2.2975	2.408
c17-28s-zsp2.5-00771	150.27863	2.27316	2.53
c17-28s-zsp2.5-01189	150.29594	2.3454	2.465
c17-28s-zsp2.5-01193	150.30426	2.33754	2.448
c17-28s-zsp2.5-01201	150.25424	2.33063	2.468
c17-28s-zsp2.5-01203	150.25378	2.32426	2.468
c17-29-zph2.3-33410	150.28709	2.41177	2.312
c17-29-zph2.5-33398	150.29295	2.42088	2.402
c17-29-zph2.5-33402	150.30779	2.41704	2.545
c17-29-zph2.6-14815	150.30571	2.39347	2.47
c17-29-zph2.6-17483	150.31509	2.49175	2.4
c17-29-zph2.6-34570	150.28142	2.48831	2.559
c17-29-zph2.7-14804	150.31004	2.39676	2.566
c17-29-zph2.8-14723	150.31305	2.45708	2.567
c17-29-zsp2.3-01174	150.25618	2.38222	2.313
c17-29-zsp2.6-01157	150.29317	2.45171	2.556
c17-62-zph2.3-14818	150.34473	2.39424	2.279
c17-62-zph2.4-14776	150.37248	2.41991	2.471
c17-62-zph2.4-17503	150.33798	2.47542	2.403
c17-62-zph2.5-14742	150.32265	2.44352	2.505
c17-62-zph2.5-14763	150.32812	2.42992	2.555
c17-62-zph2.6-14751	150.31796	2.43698	2.551
c17-62-zph2.7-17517	150.3484	2.46721	2.587
c17-62-zsp2.5-01159	150.35135	2.44302	2.452
c17-62-zsp2.5-01168	150.31071	2.40391	2.496
c17-62-zsp2.5-01502	150.3588	2.48178	2.471
c17-62-zsp2.5-01512	150.35596	2.4634	2.471
c17-61L-zph2.5-14882	150.34009	2.35964	2.452
c17-61L-zph2.5-15010	150.32918	2.30061	2.317
c17-61L-zph2.5-32231	150.32224	2.28384	2.586
c17-61L-zph2.6-12224	150.31772	2.28078	2.534
c17-61L-zph2.6-14940	150.36411	2.33619	2.494
c17-61L-zph2.6-15018	150.37976	2.29622	2.496
c17-61L-zph2.6-33462	150.37938	2.33715	2.498
c17-61L-zph2.8-32238	150.38272	2.2858	2.658
c17-61L-zsp2.5-01187	150.35432	2.35273	2.453
c17-61L-zsp2.6-00767	150.31223	2.27923	2.578

Table A1
(Continued)

CLAMATO ID	R.A.	Decl.	z
c17-61L-zsp2.7-01205	150.34872	2.32137	2.657
c17-61L-zsp2.7-01212	150.37012	2.30588	2.655
c17-60L-zph2.3-32330	150.35461	2.14912	2.272
c17-60L-zph2.5-12291	150.35986	2.24675	2.455
c17-60L-zph2.5-12400	150.32335	2.18807	2.502
c17-60L-zph2.6-12359	150.36682	2.21295	2.483
c17-60L-zph2.6-12375	150.32465	2.20695	2.49
c17-60L-zph2.6-12432	150.36377	2.16507	2.576
c17-60L-zph2.6-32321	150.36781	2.15833	2.614
c17-60L-zph2.7-12334	150.38455	2.22249	2.728
c17-60L-zph2.9-32309	150.31273	2.17346	2.67
c17-60L-zsp2.3-00826	150.31908	2.16216	2.313
c17-60L-zsp2.5-00794	150.31914	2.22503	2.493
c17-60L-zsp2.6-00819	150.37843	2.17079	2.551
c17-60L-zsp2.6-01719	150.31601	2.24457	2.583
c17-60L-zsp2.7-00788	150.39108	2.24033	2.738
c17-60L-zsp2.7-00802	150.34006	2.20841	2.729
pc22L-zph2.3-17733	150.14896	2.4883	2.38
pc22L-zph2.5-26344	150.10031	2.46256	2.477
pc22L-zph2.8-33515	150.15773	2.4089	2.463
p18-zph2.5-15320	150.00002	2.42489	2.63
p18-zph2.6-15055	150.0636	2.42693	2.52
p18-zph2.7-34724	150.05705	2.4823	2.392
p18-zsp2.4-01220	150.06973	2.45253	2.423
p15l-zph2.5-15385	149.94215	2.36591	2.477
p15l-zph2.5-15435	149.95938	2.33549	2.506
p15l-zph2.6-33610	149.99947	2.33633	2.583
p15l-zsp2.6-01875	149.93594	2.29014	2.552
p15l-zsp2.7-01354	149.94077	2.30644	2.681

Table A2
τ_{eff} Values and Corresponding 1D Errors for the z_{low} and z_{high} Redshift Interval

z	τ_{eff}	τ_σ
2.0285	0.2115	0.0926
2.0315	0.0508	0.0761
2.0345	0.0128	0.0736
2.0376	0.0628	0.088
2.0406	0.0167	0.0763
2.0437	0.0372	0.0801
2.0467	0.1107	0.0932
2.0497	0.0136	0.084
2.0528	0.1023	0.0828
2.0742	0.1106	0.078
2.0773	0.0145	0.0741
2.0804	0.237	0.0857
2.0835	0.2226	0.086
2.0866	0.1933	0.0822
2.0897	0.1386	0.0682
2.0928	0.1717	0.0686
2.0958	0.061	0.071
2.0989	0.1111	0.0719
2.102	0.2439	0.0763
2.1052	0.2527	0.0732
2.1083	0.2786	0.0772
2.1114	0.3183	0.0822
2.1145	0.1146	0.0651
2.1176	0.0425	0.0682
2.1207	0.0495	0.0684
2.1238	0.1718	0.0663
2.127	0.152	0.0657

Table A2
(Continued)

z	τ_{eff}	τ_σ
2.1301	0.2382	0.0723
2.1332	0.0281	0.0759
2.1364	0.3557	0.0854
2.1395	0.3383	0.0831
2.1426	0.3668	0.0716
2.1458	0.3355	0.0665
2.1489	0.279	0.0623
2.1997	0.2233	0.058
2.2029	0.2031	0.0545
2.2061	0.3617	0.0625
2.2094	0.3471	0.0649
2.2126	0.1102	0.0527
2.2158	0.0969	0.0503
2.219	0.1706	0.0533
2.2222	0.2714	0.0616
2.2254	0.1884	0.0541
2.2449	0.1062	0.0486
2.2481	0.0974	0.0498
2.2677	0.1961	0.0565
2.2709	0.146	0.052
2.2742	0.098	0.0474
2.2775	0.1193	0.0455
2.2808	0.1897	0.0492
2.284	0.1481	0.0488
2.2873	0.1862	0.0438
2.2906	0.2515	0.0533
2.2939	0.1222	0.046
2.2972	0.2033	0.0458
2.3005	0.1946	0.0572
–	–	–
2.1566	0.3301	0.0692
2.1597	0.3741	0.0739
2.1629	0.196	0.0678
2.1661	0.2386	0.0635
2.1692	0.2195	0.0617
2.1724	0.0898	0.0631
2.1756	0.1067	0.0584
2.1787	0.0725	0.0618
2.1819	0.1125	0.0601
2.1851	0.0345	0.0557
2.2075	0.1165	0.0516
2.2107	0.0854	0.061
2.2139	0.1759	0.0558
2.2171	0.1038	0.0536
2.2204	0.2195	0.0607
2.2236	0.1268	0.0482
2.2268	0.11	0.0584
2.23	0.2422	0.0587
2.2333	0.1673	0.0534
2.2365	0.2795	0.0576
2.2397	0.1813	0.0534
2.243	0.247	0.0515
2.2462	0.1324	0.051
2.2495	0.0812	0.0458
2.2527	0.0554	0.0523
2.256	0.0118	0.0503
2.2592	0.0793	0.0481
2.2625	0.0745	0.0489
2.2658	0.128	0.057
2.269	−0.0031	0.0505
2.2723	0.182	0.0436
2.2756	0.2785	0.05
2.2789	0.2218	0.0582
2.2821	0.2094	0.0561

Table A2
(Continued)

z	$\tau_{\rm eff}$	τ_{σ}
2.2854	0.2975	0.0498
2.3384	0.2053	0.0461
2.3418	0.2232	0.0447
2.3451	0.3334	0.0586
2.3485	0.3247	0.0542
2.3518	0.2601	0.0509
2.3552	0.098	0.0411
2.3585	0.2244	0.055
2.3619	0.1617	0.05
2.3652	0.1963	0.0481
2.3855	0.0616	0.0463
2.3889	0.0763	0.0377
2.4093	0.1726	0.0505
2.4127	0.204	0.0465
2.4161	0.215	0.0362
2.4195	0.1851	0.0385
2.4229	0.1438	0.0376
2.4264	0.1895	0.04
2.4298	0.1142	0.0431
2.4332	0.1336	0.04
2.4367	0.1676	0.0468
2.4401	0.1135	0.0408
2.4436	0.1519	0.0428
2.447	0.0025	0.0363

Note. The latter's values are appended to the former's and are separated by a row of dashes.

ORCID iDs

Jose S. Monzon https://orcid.org/0000-0002-9986-4604
J. Xavier Prochaska https://orcid.org/0000-0002-7738-6875
Khee-Gan Lee https://orcid.org/0000-0001-9299-5719
John Chisholm https://orcid.org/0000-0002-0302-2577

References

Becker, G. D., Hewett, P. C., Worseck, G., & Prochaska, J. X. 2013, MNRAS, 430, 2067
Becker, G. D., Rauch, M., & Sargent, W. L. W. 2007, ApJ, 662, 72
Bernardi, M., Sheth, R. K., SubbaRao, M., et al. 2003, AJ, 125, 32
Calzetti, D., Armus, L., Bohlin, R. C., et al. 2000, ApJ, 533, 682
Cardelli, J. A., Clayton, G. C., & Mathis, J. S. 1989, ApJ, 345, 245
Chisholm, J., Rigby, J. R., Bayliss, M., et al. 2019, ApJ, 882, 182
Chisholm, J., Tremonti, C. A., Leitherer, C., et al. 2015, ApJ, 811, 149
Dall'Aglio, A., Wisotzki, L., & Worseck, G. 2008, A&A, 491, 465
de Mello, D. F., Leitherer, C., & Heckman, T. M. 2000, ApJ, 530, 251
Faucher-Giguere, C.-A., Prochaska, J. X., Lidz, A., Hernquist, L., & Zaldarriaga, M. 2008, ApJ, 681, 831
Green, G. M., Schlafly, E. F., Finkbeiner, D., et al. 2018, MNRAS, 478, 651
Gunn, J. E., & Peterson, B. A. 1965, ApJ, 142, 1633
Hassan, S., Finlator, K., Davé, R., Churchill, C. W., & Prochaska, J. X. 2020, MNRAS, 492, 2835
Kirkman, D., Tytler, D., Suzuki, N., et al. 2005, MNRAS, 360, 1373
Kriek, M., Shapley, A. E., Reddy, N. A., et al. 2015, ApJS, 218, 15
Le Fevre, O. 2015, IAUGA, 29, 2258239
Lee, K.-G., Hennawi, J. F., White, M., Croft, R., & Ozbek, M. 2014, ApJ, 788, 49
Lee, K.-G., Krolewski, A., White, M., et al. 2018, ApJS, 237, 31
Leitherer, C., Schaerer, D., Goldader, J. D., et al. 1999, ApJS, 123, 3
Leitherer, C., Tremonti, C. A., Heckman, T. M., & Calzetti, D. 2011, AJ, 141, 37
Lilly, S. J., Le Fèvre, O., Renzini, A., et al. 2007, ApJS, 172, 70
Markwardt, C. B. 2009, in ASP Conf. Ser. 411, Non-linear Least-squares Fitting in IDL with MPFIT, ed. D. A. Bohlender, D. Durand, & P. Dowler (San Francisco, CA: ASP), 251
McDonald, P., Seljak, U., Burles, S., et al. 2006, ApJS, 163, 80
McQuinn, M. 2016, ARA&A, 54, 313
Meiksin, A. A. 2009, RvMP, 81, 1405
Nanayakkara, T., Glazebrook, K., Kacprzak, G. G., et al. 2016, ApJ, 828, 21
O'Donnell, J. E. 1994, ApJ, 422, 158
Oke, J. B., Cohen, J. G., Carr, M., et al. 1995, PASP, 107, 375
Paris, I., Petitjean, P., Rollinde, E., et al. 2011, A&A, 530, A50
Prochaska, J. X., Worseck, G., & O'Meara, J. M. 2009, ApJL, 705, L113
Rauch, M. 1998, ARA&A, 36, 267
Reddy, N. A., Steidel, C. C., Pettini, M., et al. 2008, ApJS, 175, 48
Reddy, N. A., Steidel, C. C., Pettini, M., & Bogosavljevic, M. 2016, ApJ, 828, 107
Rix, S. A., Pettini, M., Leitherer, C., et al. 2004, ApJ, 615, 98
Schaye, J., Aguirre, A., Kim, T., et al. 2003, ApJ, 596, 768
Scoville, N., Aussel, H., Brusa, M., et al. 2007, ApJS, 172, 1
Shapley, A. E., Steidel, C. C., Pettini, M., & Adelberger, K. L. 2003, ApJ, 588, 65
Steidel, C. C., Giavalisco, M., Pettini, M., Dickinson, M., & Adelberger, K. L. 1996, ApJL, 462, 17
Theuns, T., Bernardi, M., Frieman, J., et al. 2002, ApJL, 574, L111
Thomas, R., Le Fevre, O., Le Brun, V., et al. 2017, A&A, 597, A88
Tytler, D., O'Meara, J. M., Suzuki, N., et al. 2004, AJ, 128, 1058
Worseck, G., Prochaska, J. X., O'Meara, J. M., et al. 2014, MNRAS, 445, 1745